AIAA JOURNAL
Vol. 42, No. 11, November 2004

Parametric Study of Vortices Shed from Airfoil Vortex Generators

Bruce J. Wendt*
Modern Technologies Corporation, Middleburg Heights, Ohio 44130-6557

Extensive parametric study of vortices shed from the tips of airfoil vortex generators has been conducted to determine the dependence of initial vortex circulation and peak vorticity on elements of airfoil geometry and impinging-flow conditions. The vortex generators were symmetric airfoils examined in subsonic airflow on the surface of a straight pipe. The circulation and peak-vorticity data were derived from cross-plane velocity measurements acquired with a seven-hole probe one chord length downstream of the airfoil-trailing-edge-tip location. Circulation and peak vorticity are observed to be proportional to the freestream Mach number, the angle of attack, and the span-to-boundary-layer-thickness ratio. Unlike circulation, which decreases in monotonic fashion with increasing airfoil aspect ratio, peak vorticity is observed to increase with increasing aspect ratio, reaching a maximum before falling off at higher values. The circulation may be accurately modeled with an expression based on Prandtl's relationship between finite airfoil circulation and airfoil geometry. A correlation for the peak vorticity has been derived from a conservation relationship equating the moment at the airfoil tip to the rate of angular-momentum production of the shed vortex, modeled as a Lamb (ideal viscous) vortex, and is shown to provide excellent qualitative agreement with the observed behavior of peak vorticity.

Nomenclature

AR	=	airfoil aspect ratio
C_p	=	airfoil pressure coefficient
c	=	airfoil chord length
D	=	duct or pipe diameter
H	=	tip-vortex angular momentum
h	=	airfoil span
$k1$, $k2$, $k3$, $k4$	=	constants in the expression for tip-vortex circulation
M	=	pipe-core Mach number
R	=	pipe radius, 10.2 cm
Re	=	Reynolds number
r	=	radial coordinate
$r1$, $r2$	=	radial location where the velocity ratio ζ occurs
s	=	distance between adjacent vortex generators
t	=	time
v	=	velocity
v_r, v_θ, v_z	=	radial, circumferential, and axial velocity components, respectively
v_∞	=	freestream or pipe-core velocity
y	=	airfoil span coordinate
z	=	axial coordinate
α	=	airfoil angle of attack
β	=	$[2\zeta^2(1-e^{-1/2})^2]^{-1}$
Γ	=	tip-vortex circulation
δ	=	boundary-layer thickness at vortex-generator location
ζ	=	velocity ratio of the constrained Lamb vortex
η	=	fluid kinematic viscosity
θ	=	circumferential coordinate
ρ	=	fluid density
φ	=	a radial location defining a subregion of the radial axis
ω_z, $\omega_{\max}$	=	streamwise vorticity and peak streamwise vorticity, respectively

Presented as Paper 98-0693 at the 36th Aerospace Sciences Meeting, Reno, NV, 12–15 January 1998; received 8 July 2003; revision received 29 April 2004; accepted for publication 24 June 2004.

*Senior Research Engineer, Aerospace Propulsion Division, 7530 Lucerne Drive, Islander Two, Suite 206. Senior Member AIAA.

Introduction

MODERN design characteristics of aircraft-engine inlets, diffusers, and associated ducting include large amounts of centerline offset coupled with steep axial gradients in cross-sectional area. The operational performance of these components is degraded by the internal development of strong secondary flows and boundary-layer separations. Surface-mounted vortex generators are an effective means of alleviating these problems. Recent experimental work at the NASA John H. Glenn Research Center at Lewis Field in Cleveland, Ohio, has explored the strategy of using vortex-generator-induced flows to counter deleterious secondary-flow development and boundary-layer separation inside diffusing S-ducts of various geometries.[1–5] Dramatic improvements in exit-plane total-pressure recovery and flow distortion have been demonstrated. Figure 1 provides an example.

The diffuser in Fig. 1 is known as a "serpentine" S-duct. The name is derived from the pronounced centerline offset. The diffuser is also a "transitioning" S-duct; the cross-section of the flowpath transitions from a biconvex throat aperture to a circular engine face over an axial distance L of about $2.5D$. The area ratio (engine face to throat) was about 1.2. This duct geometry represented a subsonic inlet proposed for use in a compact unmanned combat aircraft where stealth considerations required a large centerline offset to screen the engine face from all lines of sight through the inlet cowl-plane aperture. Shown in Fig. 1 are the experimentally determined profiles of total pressure at the engine face for both the baseline duct and the duct with surface-mounted vane vortex generators axially positioned as indicated in the duct profile. The throat Mach number was 0.65, and the upstream reference total pressure was atmospheric. The numbers given in Fig. 1 indicate a 5% improvement in total pressure recovery and a 56% drop in circumferential distortion intensity. That such dramatic improvements can be obtained in this highly contoured and three-dimensional diffuser is strong testimony to the potential flow control available in simple vortex-generator vanes when used following the strategy of secondary-flow management. Formal elements of this strategy have recently been developed computationally by Anderson and Gibb[6,7] using the RNS3D code, a parabolized Navier–Stokes solver. The experimental results given in Fig. 1 were first designed computationally using the Falcon code, a Reynolds-averaged Navier–Stokes solver,[8] in a procedure detailed in Ref. 4. Common to the RNS3D and Falcon flow solvers is the manner in which the vortex-generator flow control is represented. The vortex generators are not modeled as part of the flow-surface grid; rather these features are represented by modeling the convective influence of the vortex shed from each vortex generator at an "initial" location in the flowfield grid downstream of where the airfoils would

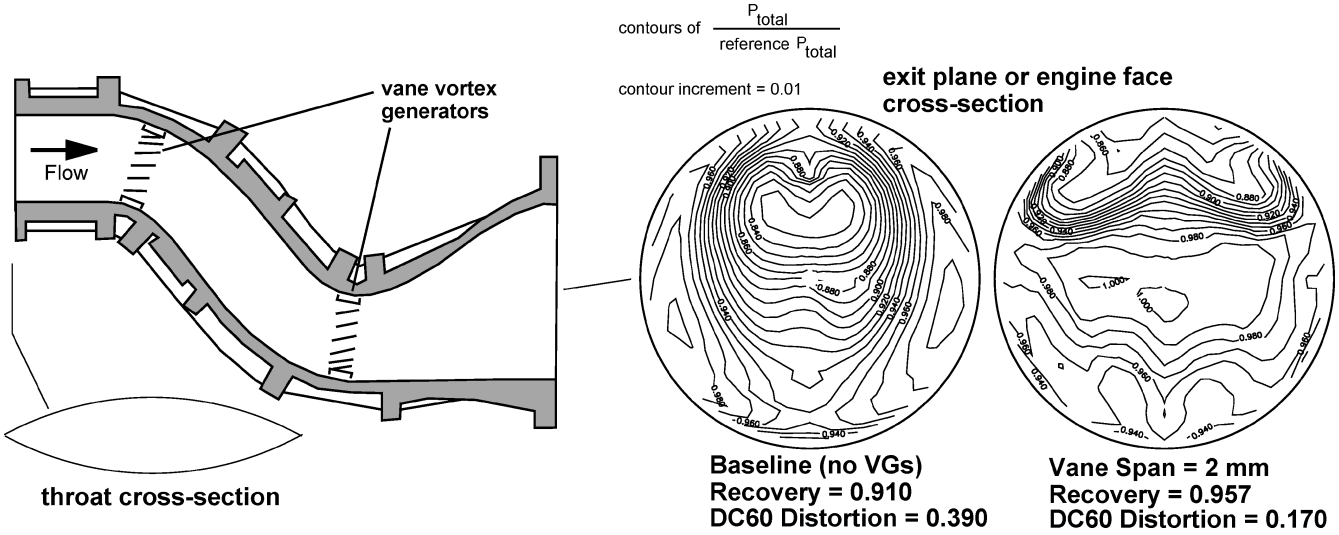

Fig. 1 Vane vortex generators dramatically improve the recovery and distortion performance of a two-turn S-diffuser.

be located in a corresponding experimental arrangement. The basis of this convective influence is found in the helical pattern of swirling flow; either the secondary velocity or the streamwise vorticity can be used.

The convective cross-plane velocity or streamwise vorticity field of the shed tip vortex may be effectively modeled over a large range of axial development using fairly simple analytical expressions. One such expression is referred to as the "Oseen" or "Lamb" vortex. This expression is obtained through classical techniques for solution of the Navier–Stokes equations simplified to represent two-dimensional axisymmetric flow.[9] Simply stated, a Lamb vortex is a time-dependent axisymmetric viscous flow that starts as a potential vortex. The velocity at the origin ($r = 0$, center of the vortex) is forced to zero at time $t = 0$. The resulting solution describes the subsequent decay. In radial coordinates, this is

$$v_\theta = (\Gamma/2\pi r)[1.0 - \exp(-r^2/4\eta t)] \tag{1}$$

In this expression, Γ is the limiting value of vortex circulation (as $r \to \infty$) and r is measured from the center of the vortex (cross-plane origin). Let z represent the streamwise or axial coordinate. Replace t with the streamwise convective displacement $t \approx z/v_\infty$ (with the origin of z coinciding with $t = 0$) and differentiate $v_\theta(r, z)$ to obtain the streamwise vorticity field:

$$\omega_z = (v_\infty \Gamma/4\pi\eta z)\exp\left\{-v_\infty r^2/4\eta z\right\} \tag{2}$$

The peak vorticity is thus $\omega_{\max} = v_\infty \Gamma/(4\pi\eta z)$. Substitute for η and t in Eq. (1) to find

$$v_\theta = (\Gamma/2\pi r)\left[1.0 - \exp\left(-\pi\omega_{\max} r^2/\Gamma\right)\right] \tag{3}$$

or, in other words, the Lamb vortex in terms of circulation and peak vorticity.[10] This form aids the modeling process, because it requires information (or data) about the vortex in the vicinity of the core only, where the circulation and peak vorticity are (for practical purposes) entirely contained. If, for example, we chose to write Eq. (3) in terms of the conserved properties of vortex cross-plane angular momentum or kinetic energy, a researcher would be required to obtain information over the entire flowfield. Another element of the modeling process is the representation of neighboring vortices and bounding flow surfaces. This may be done through the superposition (summation) of terms similar to Eq. (3). The parameters Γ, $\omega_{\max}$, and core-center location are known as "vortex descriptors," following the work of Westphal et al.[11] When combined into an expression such as Eq. (3), the resulting model accurately mimics the convective effects of a tip vortex in the cross-plane downstream of the parent vortex generator. The initial axial location where the model is placed is the position at which the formative or roll-up processes of the vortex are complete. Circulation and peak vorticity have reached maximum values here, and development further downstream leads to decay in both quantities. Previous studies[12,13] indicate that the initial location is located about one chord length downstream of the airfoil trailing edge. From this point on, the terms Γ and $\omega_{\max}$ will represent these initial values of the vortex descriptors.

Many studies have demonstrated similarities between the Lamb vortex model and the cross-plane structure of tip vortices shed from various types of vortex generators. Pauley and Eaton[14] demonstrated this in a study of delta-wing vortex generators, Wendt and Hingst[15] for low-profile wishbone vortex generators, and, more recently, Wendt et al.,[12] Wendt and Reichert,[13,16] and Wendt[17] for symmetric-airfoil-vortex generators. To complete the modeling of a vortex generator we must show how the tip-vortex descriptors depend on the geometry of the vortex generator, the influence of neighboring vortices, and the impinging-flow conditions. For airfoil-vortex generators we might express this dependence as

$$\Gamma = \Gamma(c, h, \alpha, \text{profile}, s, \delta, M, Re, \ldots)$$

$$\omega_{\max} = \omega_{\max}(c, h, \alpha, \text{profile}, s, \delta, M, Re, \ldots) \tag{4}$$

where "profile" refers to the shape of the airfoil cross section. The mathematical description of vortex generators currently used in computational codes for fluids only crudely approximates the functional dependence indicated by Eq. (4). As a means of improving current vortex-generator models, a study was undertaken to examine the effects of vortex-generator geometry (c, h, and α), spacing (s), and impinging-flow conditions for one type of airfoil vortex-generator profile: the symmetric NACA-0012. This study consisted of a series of parametric experimental tests covering a range of h/c (vortex-generator aspect ratio), h/δ, α, and M. Spacing effects were examined by considering corotating and counter-rotating pairs of vortices. The vortex generators were mounted either in isolation, in pairs, or in symmetric counter-rotating arrays spanning the full circumference of a straight pipe with diameter $D = 20.4$ cm. The impinging airstream was subsonic with a nominal turbulent-boundary-layer-thickness-to-pipe-diameter ratio $\delta/D \approx 0.09$. Three-dimensional mean-flow-velocity data were acquired in a cross-plane grid located one chord length downstream of the vortex-generator trailing edge(s). This was done using a rake of seven-hole probes or a single seven-hole probe tip. The database derived from this study contains 102 individual cross-plane surveys of tip vortices, covering 88 different airfoil-geometry, impinging-flow, and spacing configurations. This paper reports on the results for variations in vortex-generator geometry and impinging-flow conditions.

A limited set of cross-plane survey plots are presented as illustrations. Comparisons of the experimental results with expressions derived from inviscid airfoil theory and a conservation relationship are conducted to establish the Γ and ω_{max} dependence on airfoil geometry and impinging-flow conditions. Closed-form functional relationships are obtained for the limited set of parameters considered and are described below. The effects of spacing, and a complete set of survey plots (for all 102 tip vortices captured), are found in Ref. 17.

Facilities and Procedures

Test Facility and Vortex Generators

This study was conducted in the Internal Fluid Mechanics Facility (IFMF) at the NASA Glenn Research Center. The IFMF is a subsonic facility designed to investigate a variety of duct-flow phenomena. The facility, as it was configured for this test, is illustrated in Fig. 2. Air was supplied from the surrounding test cell to a large settling chamber containing a flow-straightening honeycomb and screens. At the downstream end of the settling chamber the airstream was accelerated through a contraction section to the test section. The test-section duct consisted of a straight circular pipe of inside diameter $D = 20.4$ cm. After exiting the test section duct, the airstream was routed to a discharge plenum, which was continuously evacuated by the laboratory's central exhauster facilities. The Mach number at the core of the test-section duct could be set between 0.20 and 0.80 with corresponding Reynolds numbers (based on pipe diameter) between 1×10^6 and 4×10^6. Mass flows were between 3 and 7 kg/s. More information on the design and operation of the IFMF may be found in the report of Porro et al.[18]

Figure 3 is a detailed illustration of the various test-section components. A short section of straight pipe (labeled Inlet Pipe in Fig. 3) connects the exit of the facility contraction to the duct segment containing the vortex-generator airfoil(s). Static-pressure taps located on the surface of the inlet pipe allowed the nominal core Mach number in the test section to be set and monitored. The duct portion containing the vortex-generator airfoil(s) is referred to as the "vortex-generator duct." The inside surface of the vortex-generator duct (and hence the attached vortex generator) could be rotated about an axis coinciding with the test-section centerline. Full (360-deg) rotation was possible. The rotation was driven by a motor and gearbox located in an airtight box above the vortex-generator duct. A single circumferential row of vortex-generator mounting locations was contained in the vortex-generator duct as illustrated in Fig. 3. There were 12 mounting locations spaced 30 deg, apart covering the entire inside circumference of the pipe. Over most of the testing, vortex generators were mounted in isolation in just one of these locations (with the other locations being filled by contoured blanks or "plugs"). For test conditions considering the variation in pipe-core Mach number, the vortex generators were tested in full counter-rotating array (12 identical airfoils alternating in the sign of α and spaced 30 deg apart at the midchord position) configurations. This exception was necessary to balance the aerodynamic loading on the duct-traversing mechanism and actuator at the higher Mach numbers. A typical airfoil-vortex generator is illustrated in Fig. 4.

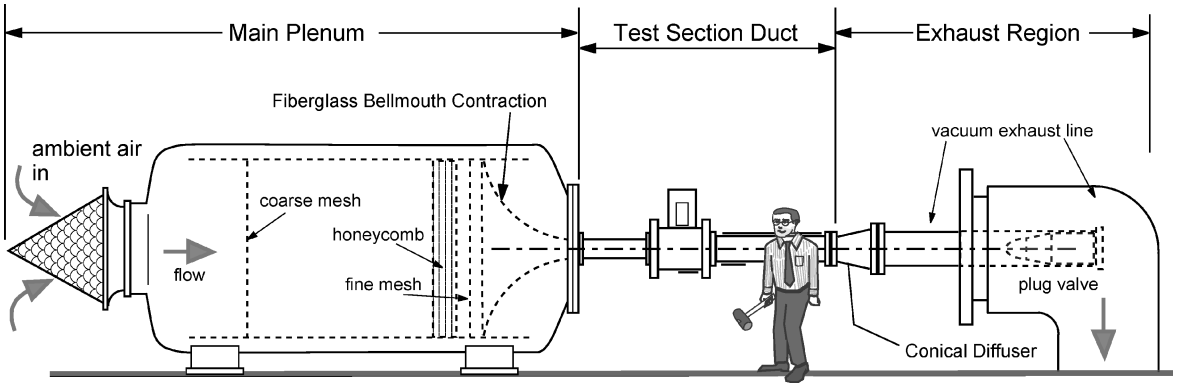

Fig. 2 Internet Fluid Mechanics Facility of NASA Glenn.

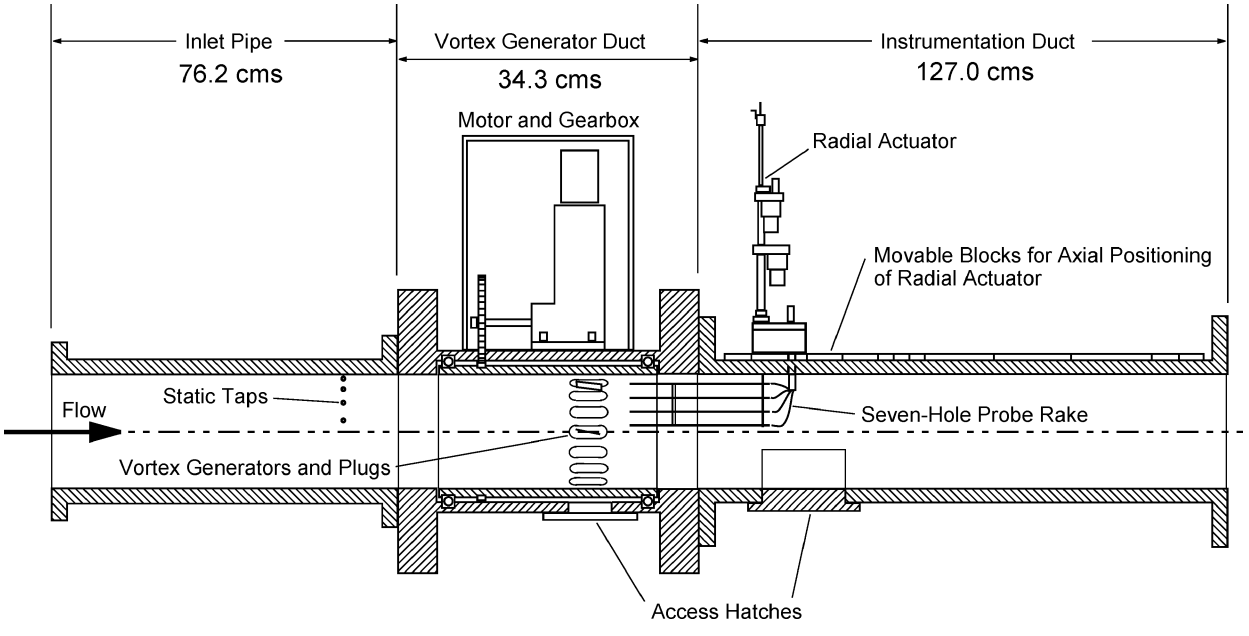

Fig. 3 Cutaway sketch of the test-section duct.

Table 1 Results for isolated airfoils and airfoils tested in full counter-rotating arrays

α, deg	c, cm	h, cm	AR	h/δ	v_∞, m/s	Mach	Γ, m^2/s	ω_{max}, 1/s
8	4.06	1.02	0.64	0.57	85	0.25	−0.291	−18193
12	4.06	1.02	0.64	0.57	85	0.25	−0.471	−24346
16	4.06	1.02	0.64	0.57	85	0.25	−0.643	−33189
20	4.06	1.02	0.64	0.57	85	0.25	−0.940	−34055
16[a]	4.06	1.02	0.64	0.57	85	0.25	−0.722	−35714
16[a]	4.06	1.02	0.64	0.62	129	0.40	−1.149	−56831
16[a]	4.06	1.02	0.64	0.65	187	0.60	−1.724	−84000
16	0.85	0.21	0.64	0.12	85	0.25	−0.156	−20297
16	0.85	0.51	1.53	0.29	85	0.25	−0.240	−22340
16	0.85	1.02	3.06	0.57	85	0.25	−0.253	−30881
16	0.85	1.52	4.58	0.86	85	0.25	−0.297	−33368
16	0.85	2.03	6.11	1.14	85	0.25	−0.307	−38301
16	1.36	0.28	0.64	0.19	85	0.25	−0.223	−29194
16	1.36	0.51	0.96	0.29	85	0.25	−0.342	−23734
16	1.36	0.81	1.53	0.46	85	0.25	−0.315	−42509
16	1.36	1.02	1.91	0.57	85	0.25	−0.315	−35415
16	1.36	1.52	2.86	0.86	85	0.25	−0.429	−37397
16	1.36	1.63	3.06	0.91	85	0.25	−0.419	−52295
16	1.36	2.03	3.82	1.14	85	0.25	−0.485	−50676
16	1.36	2.54	4.78	1.43	85	0.25	−0.428	−44093
16	1.36	3.05	5.73	1.71	85	0.25	−0.476	−60375
16	1.36	3.56	6.68	2.00	85	0.25	−0.446	−63832
16	2.03	0.51	0.64	0.29	85	0.25	−0.322	−27772
16	2.03	1.02	1.27	0.57	85	0.25	−0.435	−43956
16	2.03	1.22	1.53	0.69	85	0.25	−0.493	−52181
16	2.03	1.52	1.91	0.86	85	0.25	−0.552	−57278
16	2.03	2.03	2.55	1.14	85	0.25	−0.596	−56235
16	2.03	2.44	3.06	1.37	85	0.25	−0.667	−44619
16	2.54	0.51	0.51	0.29	85	0.25	−0.450	−22914
16	2.54	0.64	0.64	0.36	85	0.25	−0.421	−31387
16	2.54	1.02	1.02	0.57	85	0.25	−0.525	−43913
16	2.54	1.52	1.53	0.86	85	0.25	−0.626	−57104
16	2.54	2.03	2.04	1.14	85	0.25	−0.719	−73333
16	2.54	2.54	2.55	1.43	85	0.25	−0.781	−58750
16	2.54	3.05	3.06	1.71	85	0.25	−0.825	−42748
16	2.54	3.56	3.56	2.00	85	0.25	−0.862	−46882
16	2.54	4.57	4.58	2.57	85	0.25	−0.866	−70289
16	3.05	0.51	0.42	0.29	85	0.25	−0.399	−23345
16	3.05	0.76	0.64	0.43	85	0.25	−0.530	−30924
16	3.05	1.02	0.85	0.57	85	0.25	−0.591	−40099
16	3.05	1.52	1.27	0.86	85	0.25	−0.704	−53251
16	3.05	1.83	1.53	1.03	85	0.25	−0.776	−59852
16	3.05	2.03	1.70	1.14	85	0.25	−0.817	−58695
16	3.05	3.66	3.06	2.06	85	0.25	−0.985	−35505
							±5%	±7%
16	3.56	0.51	0.36	0.29	85	0.25	−0.451	−21114
16	3.56	0.89	0.64	0.50	85	0.25	−0.662	−36897
16	3.56	1.02	0.73	0.57	85	0.25	−0.648	−40085
16	3.56	1.52	1.09	0.86	85	0.25	−0.780	−54079
16	3.56	2.03	1.46	1.14	85	0.25	−0.944	−59439
16	3.56	2.13	1.53	1.20	85	0.25	−0.941	−67331
16	3.56	4.27	3.06	2.40	85	0.25	−1.170	−45710
16	4.06	0.51	0.32	0.29	85	0.25	−0.429	−19956
16	4.06	1.02	0.64	0.57	85	0.25	−0.713	−39161
16	4.06	1.52	0.96	0.86	85	0.25	−0.824	−50476
16	4.06	2.03	1.27	1.14	85	0.25	−0.961	−60834
16	4.06	2.44	1.53	1.37	85	0.25	−1.044	−63493
16	4.06	2.54	1.59	1.43	85	0.25	−1.045	−66113
16	4.06	3.05	1.91	1.71	85	0.25	−1.210	−66124
16	4.06	3.56	2.23	2.00	85	0.25	−1.243	−69638
							±5%	±7%

[a]Data from full counter-rotating airfoil arrays.

These vortex generators consisted of an airfoil-shaped blade (with a NACA-0012 profile, flat end-cap) mounted perpendicular to the surface of a base plug. The surface of the base plug was contoured to the inside radius of the vortex-generator duct. Both the blade and plug were machined from an aluminum alloy using a wire-cutting (electric-discharge-machining) process. Table 1 provides the detailed geometry of all vortex generators used in this study.

Instrumentation and Procedures

The coordinate system used in this study originated in the vortex-generator duct. The axial location, $z = 0$, coincided with the trailing edge of the vortex-generator or vortex-generator array. All surveys conducted in this study were carried out in the r–θ cross plane at axial location $z = 1$ chord length. The duct segment downstream of the vortex-generator duct was stationary (nonrotating). This test-section segment was referred to as the "instrumentation duct" and is illustrated in Fig. 3. The cross-plane flowfield measurements were acquired in this duct (at the 12 o'clock position) through the use of either a radially actuated rake probe containing four equally spaced seven-hole probe tips (shown in Fig. 3) or a single radially actuated seven-hole probe tip. These probe tips were calibrated in accordance with the procedure outlined by Everett et al.[19] The flow-angle range

covered in calibration was ±40 deg in both pitch and yaw. Uncertainty in flow-angle measurement was ±0.7 deg in either pitch or yaw, for flow-angle magnitude below 35 deg (pitch and yaw flow-angle magnitude rarely exceeded 35 deg in this study). The corresponding uncertainty in velocity magnitude was approximately ±1% of the core velocity, v_∞. The pressure data used to establish this velocity were acquired at each grid point by averaging multiple measurements taken over a time interval (10 s) much longer than any perceived unsteadiness in the flowfield. To acquire data in the r–θ cross plane the rake probe, or single probe, was actuated over a certain radial segment along the vertical line extending from duct wall to pipe center. The vortex-generator-duct flow surface and vortex generator(s) were then rotated an increment in circumferential position, $\Delta\theta$, and the radial survey was repeated. In this manner, the rake probe would acquire pie-shaped pieces of the flowfield, and the single probe would acquire ring-segment-shaped pieces. The circumferential and radial extent of the survey grid was determined by the requirement that the viscous core of the vortex be fully captured. This allowed the calculation of Γ and $\omega_{\max}$, as explained below. In most cases, the circumferential extent of the survey grid was about 15 deg, and the radial extent was about 0.700 cm. Grid resolution was $\Delta\theta = 1$ deg and $\Delta r = 1.3$ mm. The boundary-layer thickness (δ) at $z = 0$ was measured in the absence of the vortex generators, using the rake of seven-hole probes. Boundary-layer profiles were acquired for Mach numbers of 0.25, 0.40, and 0.60 with resulting values of turbulence $\delta = 1.78$, 1.65, and 1.57 cm, respectively.[13] The ratio of probe-tip diameter to vortex-viscous-core diameter varied from about 0.10 to 0.25. This small relative probe size, coupled with the close proximity of the measurement plane to the vortex-generator tip (always one chord length), indicated that measurement errors due to probe interference and possible vortex-core wandering were negligible.[20]

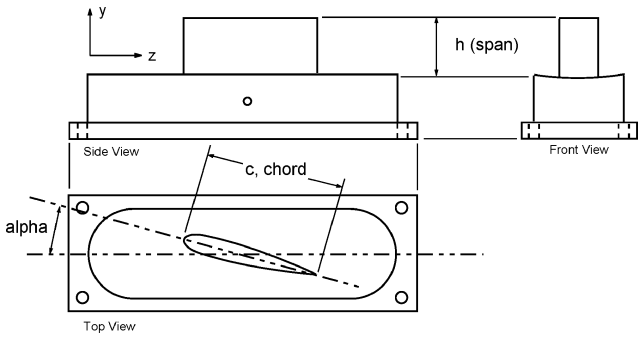

Fig. 4 Geometry of the airfoil vortex generator.

Experimental Results

Fifty-nine individual cross-plane surveys were conducted to explore the influence of v_z, α, c, and h on the structure of the tip vortex. Figure 5 is an illustration of the results obtained in six surveys conducted behind vortex-generator airfoils with $c = 3.56$ cm. This figure clearly shows the progression of the tip vortex away from the wall as the aspect ratio (AR) of the airfoil is increased. Figure 5 is a subset of the data plots found in Ref. 17. The vector plots at the top are the measured values of secondary velocity, the plots in the center are the corresponding measured axial-velocity contours, and the plots at the bottom are the derived contours of streamwise vorticity. The radial axis of each plot represents distance from the wall, R–r. The circumferential axis represents angular position in degrees. To obtain the streamwise vorticity from the measurements,

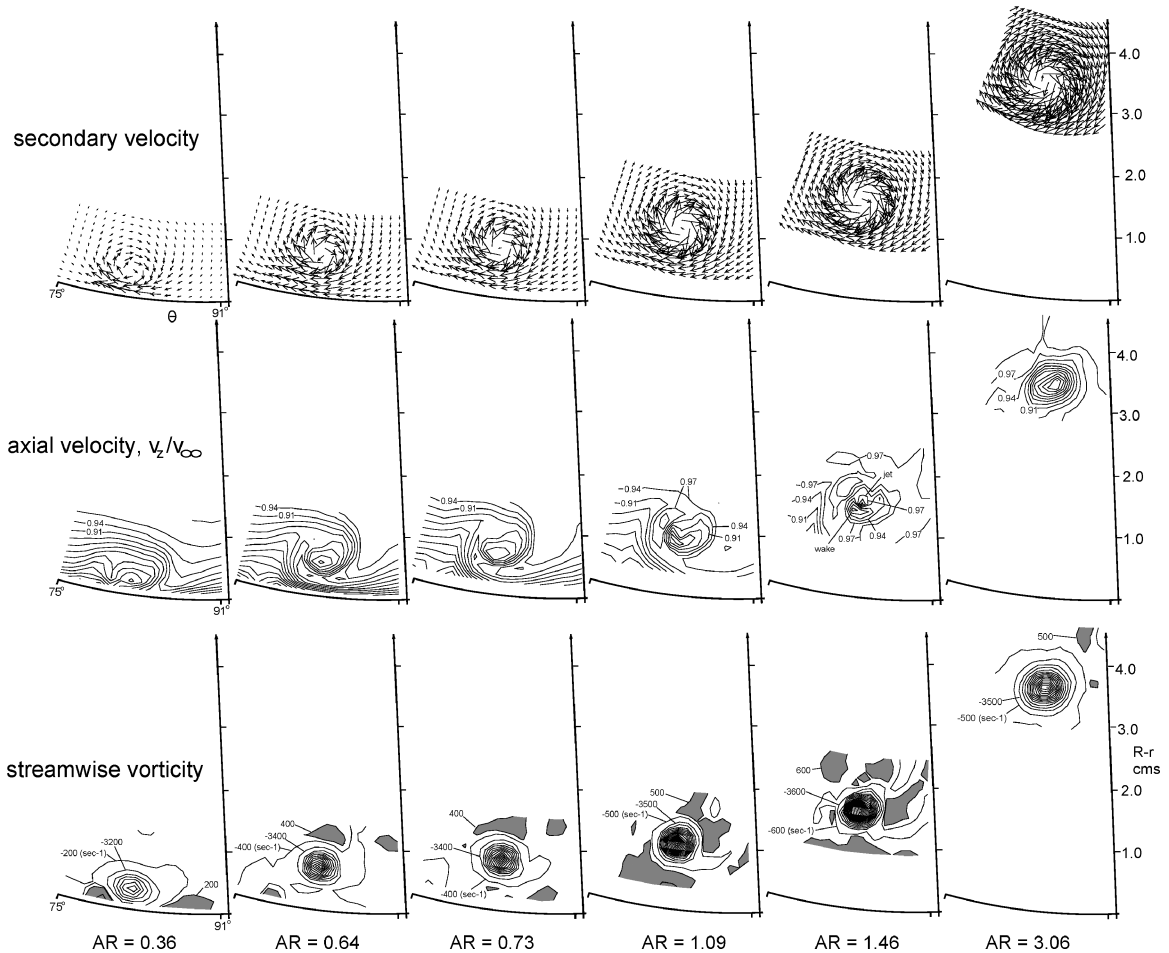

Fig. 5 Velocity and streamwise vorticity results for variation in airfoil aspect ratio chord length = 3.56 cm, α = 16 deg, and pipe core Mach number = 0.25.

we first convert the secondary velocity data following the relation

$$\omega_z = \frac{\partial v_\theta}{\partial r} + \frac{v_\theta}{r} - \frac{1}{r}\frac{\partial v_r}{\partial \theta} \tag{5}$$

Finite difference formulas were used to represent the spatial derivatives in Eq. (5). In the plots of streamwise vorticity of Fig. 5, contour lines surrounding unshaded regions represent negative values of vorticity; lines surrounding shaded regions represent positive values of vorticity. The contour increment for lines not labeled is $\pm 3000\ \mathrm{s}^{-1}$. The peak vorticity was located at some grid point having coordinates (r_c, θ_c). Circulation was calculated by first isolating the region of core vorticity in the data field. This was done by plotting the "bounding value" contour of core vorticity $\omega_{zb} = 0.01\omega_{max}$, as is done in the streamwise vorticity plots of Fig. 5. Circulation was then calculated according to the relation

$$\Gamma = \iint_{\substack{\text{core area inside} \\ \text{bounding contour}}} \omega_z \, \mathrm{d(area)} \tag{6}$$

where ω_z is the streamwise vorticity at each elemental cross-plane area within the ω_{zb} contour. In all cases considered here, the core had a well-defined circular or elliptical shape, and so Γ was easily determined. The tip-vortex-descriptor results for all variations in v_z, α, c, and h are listed in Table 1. Uncertainty estimates for the calculated descriptors are included. These were derived by combining the uncertainties in measured velocity and probe placement in accordance with the procedure outlined by Moffat.[21]

The complex structure of the tip vortex in the near-field region of the airfoil is a subject still undergoing intense investigation (see Refs. 20 and 22–24 for other recent experimental results). Of particular interest here are the structural features revealed by the contour plots of axial-velocity ratio, v_z/v_∞, in Fig. 5. These plots illustrate the vortex–airfoil wake–boundary layer interaction as well as some unexpected features of the tip-vortex core. Three distinct types of core structure are noted and occur according to airfoil aspect ratio:

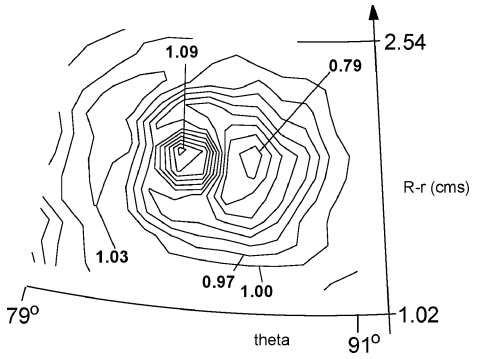

Fig. 6 Core of a tip vortex shed from an airfoil vortex generator.

1) For AR in the range $0.3 \le AR \le 1.2$ (refer to the first four axial-velocity plots in Fig. 5), the core region appears as a small circular wake buried within the boundary layer. On the right-hand side of the core, the boundary layer is thinned in the downwash of the vortex; on the left-hand side, it is thickened by the upwash. From the right-hand side, a tongue of high-momentum fluid wraps under the core region and extends up the left-hand side, creating a steep gradient in the axial velocity field in the upwash of the vortex.

2) For AR in the range $1.2 \le AR \le 2.5$ the vortex interaction with the boundary layer is considerably less (refer to the fifth plot of axial velocity in Fig. 5). A portion of the upper-boundary-layer fluid has been convected up along the left-hand side of the vortex. A dual wake-jet structure in the core is apparent. This peculiarity is found whenever the aspect ratio is in this range and the chord length is greater than 2.03 cm. The chord length restriction may simply be an artifact of probe resolution, or in other words, the tip-vortex core produced by airfoils with $c \le 2.03$ cm are too small to resolve interior features. The reasons for the jetting flow are unknown, but the fourth plot seems to indicate that the high-momentum tongue of fluid coming in from the right-hand side may be being wound-up or stretched in the rapidly swirling flow of the core. A more dramatic example is shown in Fig. 6. Here $AR = 1.59$, $c = 4.06$ cm, $h/\delta = 1.43$, and pipe-core Mach number $= 0.25$. This plot depicts a single tip-vortex core from a pair of counter-rotating vortices,[17] shown as contours of axial-velocity ratio. A wake region and a jetting region exist in close proximity within the boundary of the viscous core.

3) For AR greater than about 2.5 (refer to the last plot of axial velocity in Fig. 5) the core region is a strong circular wake with no other apparent structure. Extending below the core is the remainder of the airfoil wake.

Analysis and Modeling

A portion of the results listed in Table 1 are plotted in Figs. 7–15. The dependence of Γ and ω_{max} on α (keeping M, h/δ, and AR constant) is illustrated by Fig. 7. Both Γ (left-hand plot) and ω_{max} (right-hand plot) increase in approximate linear fashion with increasing α. The fall off in ω_{max} at large α is likely due to a flow separation on the airfoil for angles greater than about 16 deg. The dependence of Γ and ω_{max} on M (keeping α, h/δ, and AR constant) is illustrated by Fig. 8. Again the overall character of this dependence is a linear increase in the descriptors with v_∞. The dependence of Γ and ω_{max} on AR (keeping α, M, and h/δ constant) is illustrated in Figs. 9–12. Here we see Γ fall off in monotonic fashion with increasing aspect ratio. The behavior for ω_{max} is distinctly different, however. The peak vorticity first climbs to a maximum value and then falls off with increasing aspect ratio. The dependence of Γ and ω_{max} on h/δ (keeping α, M, and AR constant) is illustrated by Figs. 13–15. As expected, both Γ and ω_{max} increase with increasing h/δ. Peak vorticity, however, tails off at higher h/δ (see Fig. 14), whereas Γ does not. Also plotted on each of Figs. 7–15 are the results of analytical modeling equations developed next.

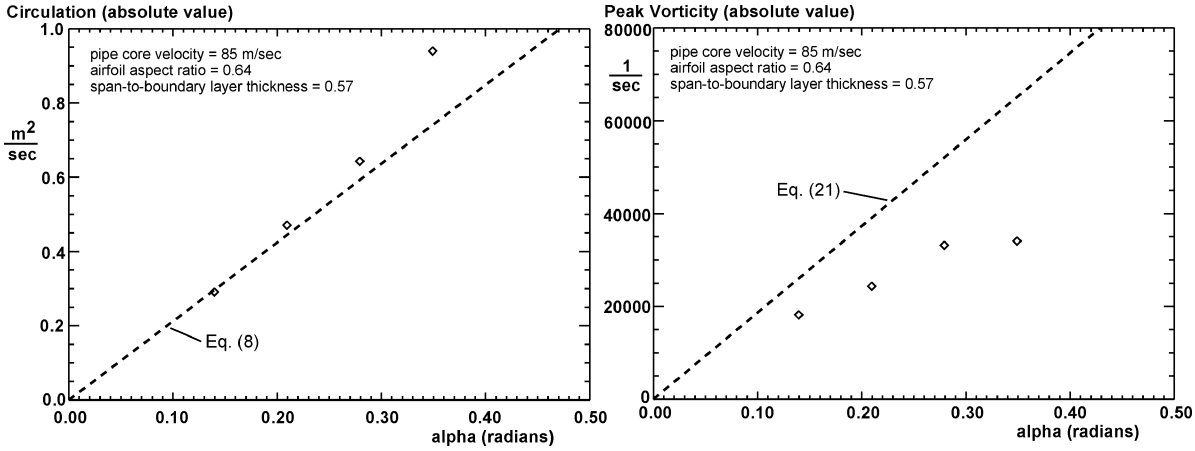

Fig. 7 Variation of circulation and peak vorticity vs airfoil angle of attack α.

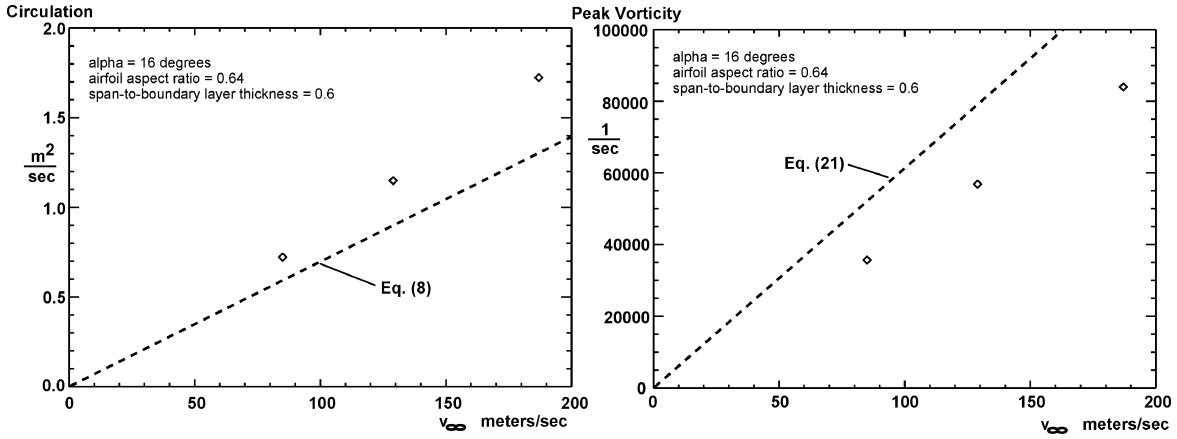

Fig. 8 Variation of circulation and peak vorticity vs pipe-core velocity.

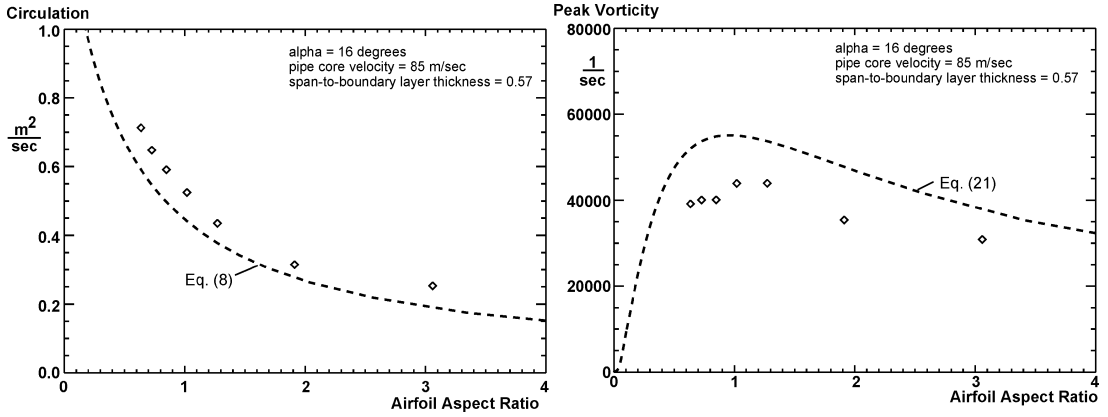

Fig. 9 Variation of circulation and peak vorticity vs airfoil aspect ratio.

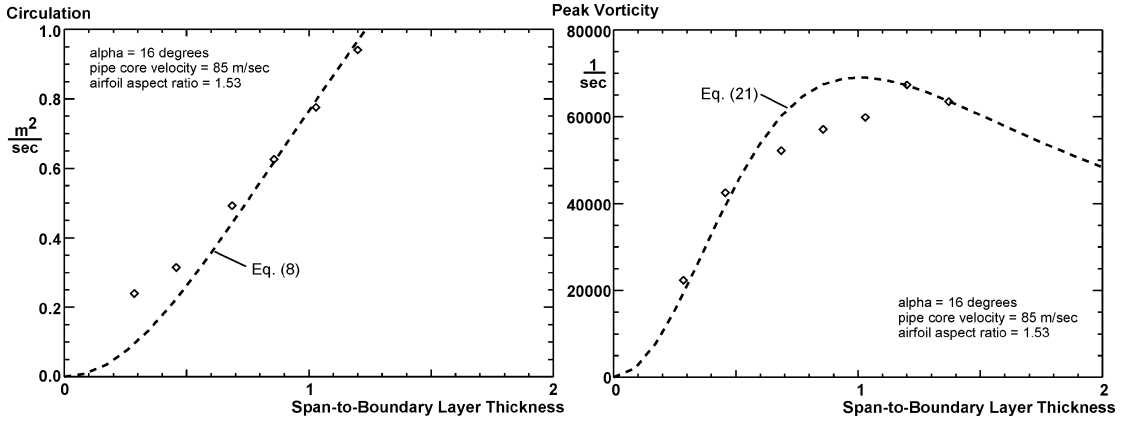

Fig. 10 Variation of circulation and peak vorticity vs span-to-boundary-layer thickness ratio.

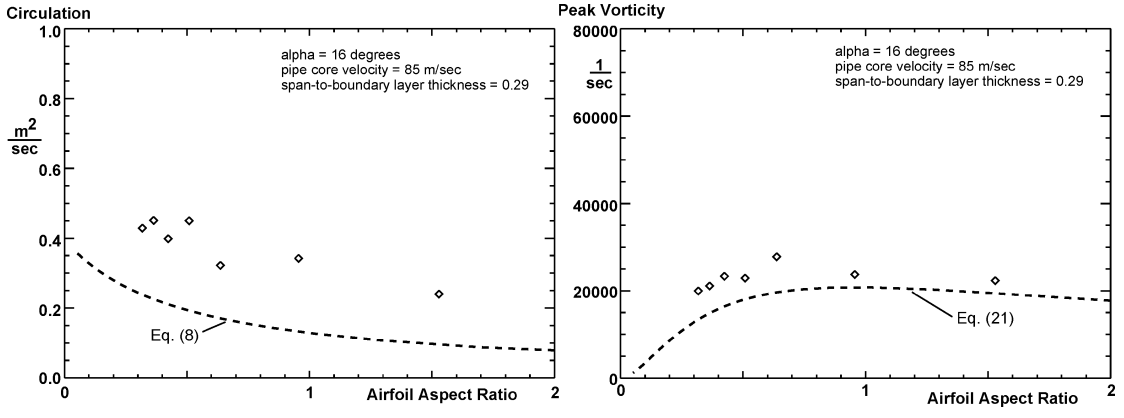

Fig. 11 Variation of circulation and peak vorticity vs airfoil aspect ratio.

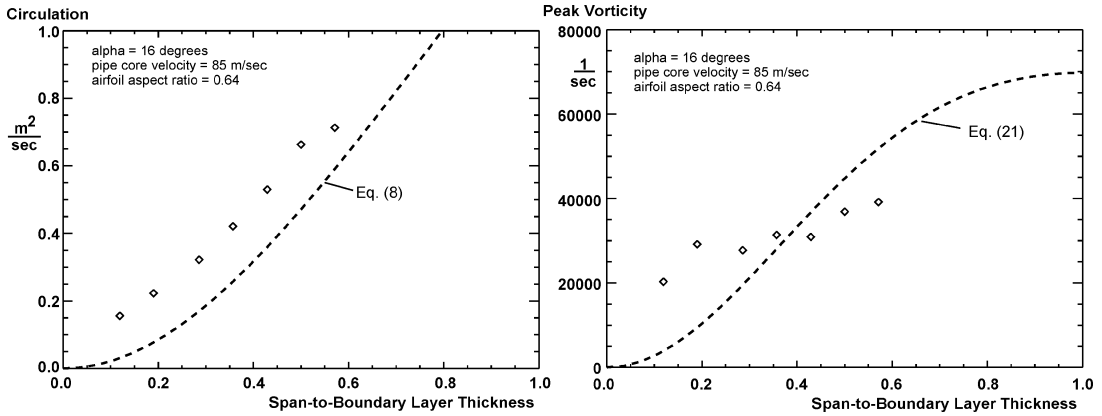

Fig. 12 Variation of circulation and peak vorticity vs span-to-boundary-layer thickness ratio.

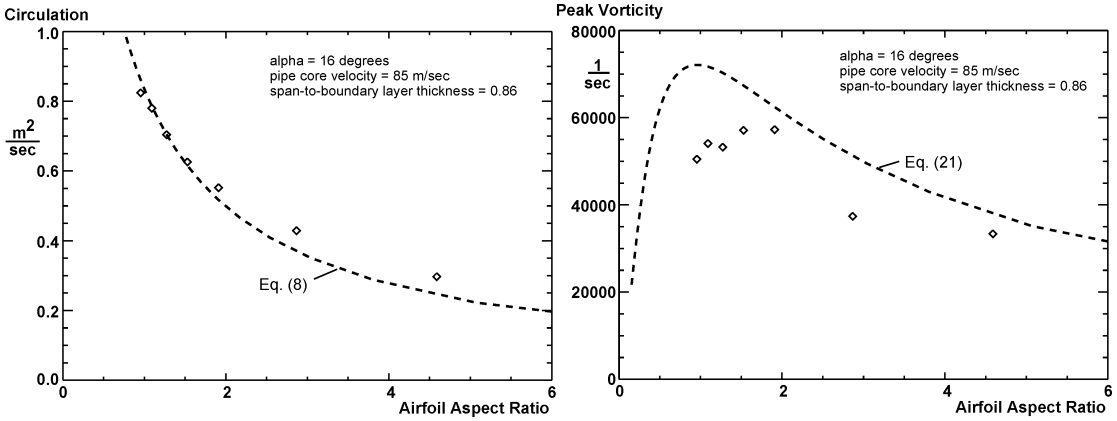

Fig. 13 Variation of circulation and peak vorticity vs airfoil aspect ratio.

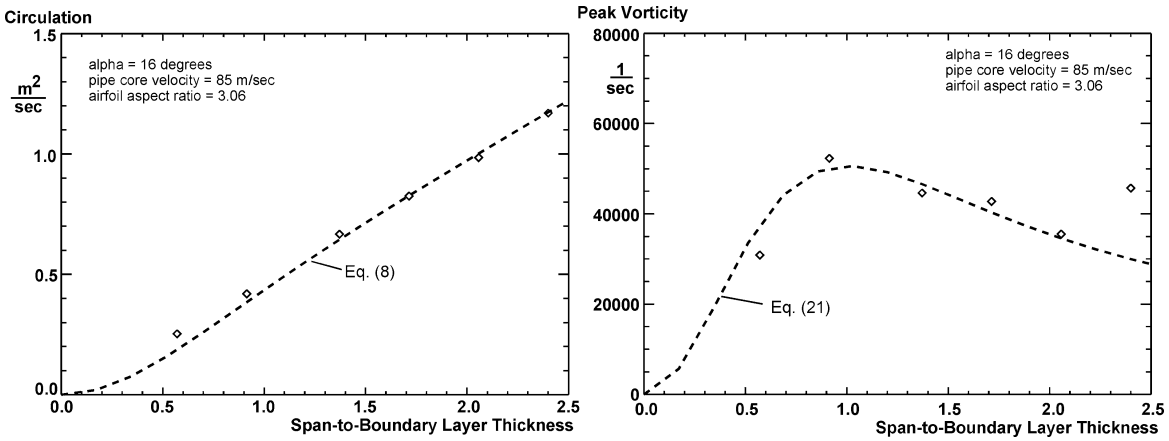

Fig. 14 Variation of circulation and peak vorticity vs span-to-boundary-layer thickness ratio.

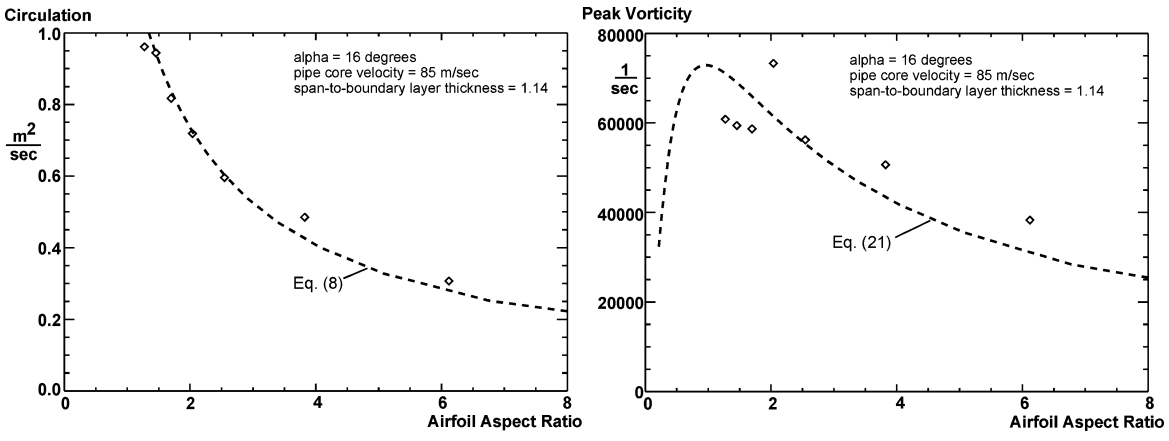

Fig. 15 Variation of circulation and peak vorticity vs airfoil aspect ratio.

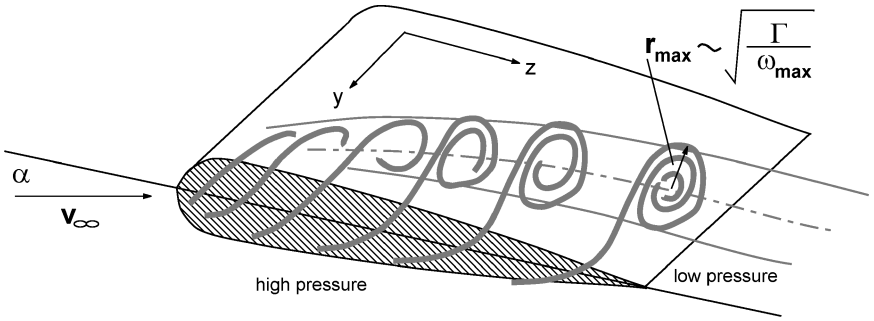

Fig. 16 Vortex rollup in the vicinity of the airfoil tip.

Circulation

The dependence of vortex circulation on vortex-generator geometry and impinging-flow conditions can be approximated with an expression developed by Prandtl.[25] For a finite-span wing of elliptical planform and symmetric cross section, the circulation developed about the wing in the plane containing the wing cross-sectional profile is

$$\Gamma = \frac{\pi v_\infty \alpha c}{1 + 2/\mathrm{AR}} \tag{7}$$

The aspect-ratio parameter defined in this study, $\mathrm{AR} = 8h/(\pi c)$, is constructed to represent wings of elliptical planform. This definition is also used in this study to represent the AR of the rectangular-planform vortex-generator airfoil. If we now assume that the circulation developed about the wing cross section is turned into the stream, Eq. (7) forms the basis for an expression approximating the circulation of the shed tip vortex:

$$\Gamma = \frac{k_1 \alpha v_\infty c}{1 + k_2/\mathrm{AR}} \tanh\left[k_3 (h/\delta)^{k_4}\right] \tag{8}$$

where k_1 and k_2 replace the constants π and 2 in Eq. (7), and the hyperbolic tangent function is used to represent the retarding influence of the boundary layer. The constants k_1 through k_4 are determined using least-squares regression with the data plotted in Figs. 7–15. The values are determined to be

$$k_1 = 1.61, \qquad k_2 = 0.48, \qquad k_3 = 1.41, \qquad k_4 = 1.00$$

Equation (8) is plotted against the circulation data in Figs. 7–15. In Figs. 7–10 and 13–15 we see close agreement between the data and Eq. (8). For the lowest values of h/δ and AR (Figs. 11 and 12), Eq. (8) underpredicts the circulation somewhat, although the behavior of Γ versus AR and h/δ is still accurately represented.

Peak Vorticity

In accurate fashion, Prandtl's inviscid analysis provides us with an estimate of Γ. The shed vortex circulation can be viewed as the integration or summation of the streamwise-vorticity field. Peak vorticity, on the other hand, is an element of the streamwise-vorticity field's distribution or "structure." Nothing of this structure can be discerned from the inviscid analysis. In fact, it may be noted that the inviscid model of a vortex has an infinite (and therefore unphysical) value of peak vorticity at the core central location (and a zero value everywhere else). Thus to begin our analysis for $\omega_{\max}$, we discard the inviscid model and consider a viscous vortex. Perhaps the simplest model of a viscous vortex is the Lamb vortex discussed earlier and described by Eqs. (1–3). To proceed with the analysis for $\omega_{\max}$, we make the following two assumptions:

1) At the initial streamwise location of 1 chord length, the vortex structure can be accurately represented by the Lamb vortex model. As indicated earlier, many previous studies exist to support this assumption.

2) The conserved property of vortex angular momentum can be related to a pressure-force moment applied near the airfoil tip.

By integrating a suitable version of the Lamb vortex to obtain an expression for angular momentum, and through the use of Prandtl's equation for Γ [Eq. (8)], we will isolate $\omega_{\max}$ in terms of vortex-generator geometry and impinging-flow conditions. Let us start first by developing the conservation relationship.

Estimating Tip-Vortex Angular-Momentum Production

The rate of vortex angular-momentum production is equated to a moment summation taken at the airfoil tip. Figure 16 illustrates the flowfield in the region near the airfoil tip where the vortex rolls up. This figure is patterned after detailed experimental results obtained on a large-scale half-wing model with a NACA-0012 sectional profile.[26] Let H be the angular momentum of the shed vortex, CF a characteristic force tending to rotate the fluid at the wing tip, and CMA a characteristic moment arm through which the fluid is rotated:

$$\sum(\text{moments at the tip}) = \mathrm{CF} \times \mathrm{CMA} = \frac{\partial H}{\partial t} \approx v_\infty \frac{H}{\mathrm{d}z} \tag{9}$$

CF is related to the lift force on the airfoil and is estimated by integrating the two-dimensional inviscid pressure distribution,[27]

$$\Delta C_p = 4.0(\sin\alpha)\sqrt{c/z - 1} \tag{10}$$

over the surface of the airfoil,

$$\mathrm{CF} = 2.0\rho v_\infty^2 \alpha c \int_{y_{\mathrm{ll}}}^{h} \int_0^c \sqrt{\frac{c}{z} - 1}\frac{\mathrm{d}z}{c}\,\mathrm{d}y \tag{11}$$

where y_{ll} represents the lower limit on the span component of integration. By setting $y_{\mathrm{ll}} = 0$ we confine our analysis to small aspect ratios. This follows because, as the aspect ratio of the airfoil increases and the span grows out of proportion to the chord, the lift forces generated near the root (or wall location) have less of an influence at the tip. Thus, at larger aspect ratios, Eq. (11) with $y_{\mathrm{ll}} = 0$ tends to overestimate CF.

CMA is taken to be the radius of the shed vortex. We approximate this by an expression for $r_{\max}$ the radial location at which v_θ [from Eq. (3)] is maximum:

$$\mathrm{CMA} \approx r_{\max} = \sqrt{\Gamma/2\pi\omega_{\max}} \tag{12}$$

Equation (12) for CMA describes what is also known as the Rankine core radius of a viscous vortex.

We integrate Eq. (11) and substitute this resulting expression with Eq. (12) into Eq. (9) to obtain

$$\frac{\sum(\text{moments at the tip})}{\rho v_\infty} = \frac{H}{\rho\,\mathrm{d}z} \approx \pi\alpha c h v_\infty \sqrt{\frac{\Gamma}{2\pi\omega_{\max}}} \tag{13}$$

We now turn our attention to integrating the Lamb-vortex model for angular momentum H.

Angular Momentum of the Constrained Lamb Vortex

The angular momentum in a region of the polar cross plane bounded by φ: $0 \le \varphi \le r$ and θ: $0 \le \theta \le 2\pi$ is evaluated with the expression

$$\frac{H}{\rho \mathrm{d}z} = \int_0^{2\pi} \int_0^r (\boldsymbol{r} \times \boldsymbol{v}) 2\pi\varphi \, \mathrm{d}\varphi \, \mathrm{d}\theta \tag{14}$$

where the vector v represents the secondary or cross-plane velocity vector. Applying Eq. (14) to Eq. (3) provides the angular-momentum profile of the Lamb vortex:

$$H/\rho \mathrm{d}z = \Gamma\left\{r^2/2 - (\Gamma/2\pi\omega_{\max})\left[1 - \exp\left(-\pi\omega_{\max} r^2/\Gamma\right)\right]\right\} \tag{15}$$

It can be seen from this expression that the angular momentum (per unit axial dimension) is unbounded in r, or in other words, $H/(\rho \mathrm{d}z) \to \infty$ as $r \to \infty$. Thus, before we can use the Lamb vortex in this analysis, a meaningful way to constrain it (in r) must be found. One approach[28] is to define a model discontinuous in v_θ. Figure 17 diagrams this construction. Figure 17 is a plot of v_θ vs r as defined by Eq. (3) for indicated values of circulation and peak vorticity. Define a velocity ratio

$$\zeta = v_\theta / v_{\theta\,\max} \tag{16}$$

where $v_{\theta\,\max}$ is the maximum angular velocity of the Lamb vortex over the range r: $0 \le r < \infty$. As Fig. 17 indicates, this velocity ratio is realized at two radial locations on the Lamb-vortex profile, $r1$ and $r2$. Choose $r2$ to be the outer boundary of this discontinuous vortex model, referred to here as the "constrained Lamb vortex." Note, from Fig. 17, that by choosing $r2$ and $\zeta \ll 1.0$, the entire viscous core and a good portion of the inviscid outer region of the Lamb vortex are retained. Now $r2$ can be approximated:

$$r2 \approx \left[1/\zeta\left(1 - e^{-\frac{1}{2}}\right)\right]\sqrt{\Gamma/2\pi\omega_{\max}} \tag{17}$$

Apply Eq. (14) within this boundary to find

$$H/\rho \mathrm{d}z = \left(\Gamma^2/2\pi\omega_{\max}\right)[\beta - 1 + e^{-\beta}] \tag{18}$$

where

$$\beta = 1/2\zeta^2\left(1 - e^{-\frac{1}{2}}\right)^2 \tag{19}$$

Equation (18) is simplified to

$$\frac{H}{\rho \mathrm{d}z} \approx \frac{\Gamma^2(\beta - 1)}{2\pi\omega_{\max}} \tag{20}$$

Note that the angular momentum of the constrained Lamb vortex is proportional to $\Gamma^2/\omega_{\max}$. Other vortex models have been examined (both continuous and discontinuous in v_θ) to determine the angular momentum relationships and these are also found to be proportional to $\Gamma^2/\omega_{\max}$ (Ref. 28).

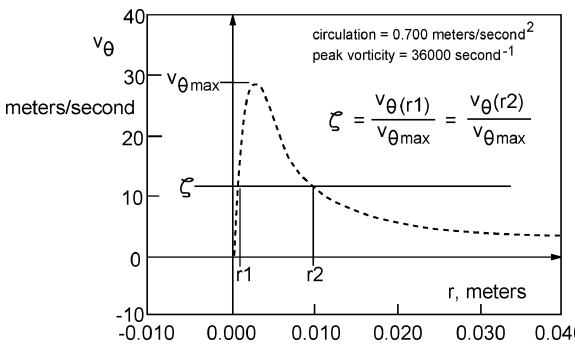

Fig. 17 Plot of angular velocity vs radial location for a Lamb vortex with given descriptors (dashed line).

Replace $H/(\rho \mathrm{d}z)$ in Eq. (13) with Eq. (20) and solve for $\omega_{\max}$ to find

$$\omega_{\max} = \frac{\Gamma^3(\beta - 1)^2}{2\pi^3\alpha^2 c^2 h^2 v_\infty^2} \tag{21}$$

The constant ζ from Eq. (16) was determined by a least-squares regression from the plotted peak-vorticity data in Figs. 7–15. The value was determined to be $\zeta = 0.29$. The peak vorticity plots (right-hand side of Figs. 7–15) illustrate the correlation of Eq. (21) with the given value of ζ. Equation (21), on the average, tends to overpredict $\omega_{\max}$ (Figs. 7–9 and 11); however, Eq. (21) also reproduces the rise and fall of $\omega_{\max}$ with increasing AR and h/δ observed in the data. Even though the scatter in the peak vorticity data is considerably greater than that seen for the circulation data, Eq. (21) clearly follows the trends indicated by the data.

Summary

An extensive parametric study of vortices shed from airfoil vortex generators has been conducted to determine the dependence of tip-vortex initial circulation and peak vorticity on airfoil angle of attack, chord length, span, impinging external Mach number, and boundary-layer thickness. The vortex generators were symmetric airfoils having NACA-0012 cross sections. These airfoils were mounted either in isolation or in full-circumference arrays (to produce counter-rotating pairs of tip vortices) on the surface of a straight pipe. The turbulent boundary-layer-thickness-to-pipe-radius ratio was $\delta/R \approx 0.17$. The circulation and peak-vorticity data were derived from cross-plane velocity measurements acquired with a seven-hole probe one chord length downstream of the airfoil trailing-edge location.

Γ is observed to be proportional to M, α, and h/δ. With these parameters held constant, Γ is observed to fall off in monotonic fashion with increasing AR. $\omega_{\max}$ is also observed to be proportional to M, α, and h/δ. Unlike Γ, however, $\omega_{\max}$ is observed to increase with increasing AR, reaching a maximum value before falling off at higher values of AR.

Γ may be accurately modeled with an expression based on Prandtl's relationship between finite airfoil circulation and airfoil geometry. A correlation for $\omega_{\max}$ has been derived from a conservation relationship equating the moment at the airfoil tip to the rate of angular-momentum production of the shed tip vortex, modeled as a Lamb (viscous) vortex. This technique provides very good qualitative agreement with the observed behavior of $\omega_{\max}$ for low-aspect-ratio airfoils typically used as vortex generators.

References

[1]Reichert, B. A., and Wendt, B. J., "Improving Diffusing S-Duct Performance by Secondary Flow Control," AIAA Paper 94-0365, Jan. 1994.

[2]Foster, J. D., Okiishi, T. H., Wendt, B. J., and Reichert, B. A., "Study of Compressible Flow Through a Rectangular-to-Semiannular Transition Duct," NASA CR-4660, April 1995.

[3]Wendt, B. J., and Dudek, J. C., "Development of Vortex Generator Use for a Transitioning High Speed Inlet," *Journal of Aircraft*, Vol. 35, No. 4, 1998, pp. 536–543.

[4]Hamstra, J. W., Miller, D. N., Truax, P. P., Anderson, B. H., and Wendt, B. J., "Active Inlet Flow Control Technology Demonstration," 22nd International Council of Aeronautical Sciences, ICAS Paper 6112, Aug. 2000.

[5]Wendt, B. J., "Suppression of Cavity-Driven Flow Separation in a Simulated Mixed Compression Inlet," NASA CR-2000-210460, Sept. 2000.

[6]Anderson, B. H., and Gibb, J., "Application of Computational Fluid Dynamics to the Study of Vortex Flow Control for the Management of Inlet Distortion," AIAA Paper 92-3177, July 1992.

[7]Anderson, B. H., and Gibb, J., "Vortex Generator Installation Studies on Steady State and Dynamic Distortion," AIAA Paper 96-3279, July 1996.

[8]Bender, E. E., Anderson, B. H., and Yagle, P. J., "Vortex Generator Modeling for Navier–Stokes Codes," American Society of Mechanical Engineers, ASME Paper FEDSM99-6919, July 1999.

[9]Panton, R. L., *Incompressible Flow*, 1st ed., Wiley, New York, 1984, pp. 283–288.

[10]Wendt, B. J., Greber, I., and Hingst, W. R., "The Structure and Development of Streamwise Vortex Arrays Embedded in a Turbulent Boundary Layer," NASA TM 105211, Sept. 1991.

[11]Westphal, R. V., Pauley, W. R., and Eaton, J. K., "Interaction Between a Vortex and a Turbulent Boundary Layer, Part 1: Mean Flow Evolution and Turbulence Properties," NASA TM 88361, Jan. 1987.
[12]Wendt, B. J., Reichert, B. A., and Foster, J. D., "The Decay of Longitudinal Vortices Shed from Airfoil Vortex Generators," AIAA Paper 95-1797, June 1995.
[13]Wendt, B. J., and Reichert, B. A., "The Modeling of Symmetric Airfoil Vortex Generators," AIAA Paper 96-0807, Jan. 1996.
[14]Pauley, W. R., and Eaton, J. K., "The Fluid Dynamics and Heat Transfer Effects of Streamwise Vortices Embedded in a Turbulent Boundary Layer," Stanford Univ. TR MD-51, Stanford, CA, Aug. 1988.
[15]Wendt, B. J., and Hingst, W. R., "Flow Structure in the Wake of a Wishbone Vortex Generator," *AIAA Journal*, Vol. 32, No. 11, 1994, pp. 2234–2240.
[16]Wendt, B. J., and Reichert, B. A., "Spanwise Spacing Effects on the Initial Structure and Decay of Axial Vortex Generators," NASA CR 198544, Nov. 1996.
[17]Wendt, B. J., "Initial Circulation and Peak Vorticity Behavior of Vortices Shed from Airfoil Vortex Generators," NASA CR 2001-211144, Aug. 2001.
[18]Porro, A. R., Hingst, W. R., Wasserbauer, C. A., and Andrews, T. B., "The NASA Lewis Research Center Internal Fluid Mechanics Facility," NASA TM 105187, Sept. 1991.
[19]Everett, K. N., Gerner, A. A., and Durston, D. A., "Seven-Hole Cone Probes for High Angle Flow Measurement: Theory and Calibration," *AIAA Journal*, Vol. 21, No. 7, 1983, pp. 992–998.
[20]Devenport, W. J., Rife, M. C., Liapis, S. I., and Follin, G. J., "The Structure and Development of a Wing-Tip Vortex," *Journal of Fluid Mechanics*, Vol. 312, April 1996, pp. 67–106.
[21]Moffat, R. J., "Contributions to the Theory of Single-Sample Uncertainty Analysis," *Journal of Fluids Engineering*, Vol. 104, June 1982, pp. 250–258.
[22]Chow, J. S., Zilliac, G. G., and Bradshaw, P., "Mean and Turbulence Measurements in the Near Field of a Wingtip Vortex," *AIAA Journal*, Vol. 35, No. 10, 1997, pp. 1561–1567.
[23]Ramaprian, B. R., and Zheng, Y., "Measurements in Rollup Region of the Tip Vortex from a Rectangular Wing," *AIAA Journal*, Vol. 35, No. 12, 1997, pp. 1837–1843.
[24]Anderson, E. A., Wright, C. T., and Lawton, T. A., "Experimental Study of the Structure of the Wingtip Vortex," AIAA Paper 2000-0269, Jan. 2000.
[25]Prandtl, L., "Applications of Modern Hydrodynamics to Aeronautics," NACA Rept. 116, Oct. 1921.
[26]Chow, J. S., Zilliac, G. G., and Bradshaw, P., "Measurements in the Near-Field of a Turbulent Wing-Tip Vortex," AIAA Paper 93-0551, Jan. 1993.
[27]Karamcheti, K., *Principles of Ideal-Fluid Aerodynamics*, 1st ed., Wiley, New York, 1966, pp. 492–516.
[28]Wendt, B. J., "Initial Peak Vorticity Behavior for Vortices Shed from Airfoil Vortex Generators," AIAA Paper 98-0693, Jan. 1998.

K. Fujii
Associate Editor